

Ultrafast quantum photonics enabled by coupling plasmonic nanocavities to strongly radiative antennas: supplementary material

SIMEON I. BOGDANOV^{1,2*}, OKSANA A. MAKAROVA^{1,2}, XIAOHUI XU^{1,2}, ZACHARIAH. O. MARTIN^{1,2}, ALEXEI S. LAGUTCHEV^{1,2}, MATTHEW OLINDE^{1,2}, DEESHA SHAH^{1,2}, SARAH N. CHOWDHURY^{1,2}, AIDAR R. GABIDULLIN^{3,4}, ILYA A. RYZHIKOV^{3,5}, ILYA A. RODIONOV^{3,4}, ALEXANDER V. KILDISHEV^{1,2}, SERGEY I. BOZHEVOLNYI⁶, ALEXANDRA BOLTASSEVA^{1,2}, VLADIMIR M. SHALAEV^{1,2*} AND JACOB B. KHURGIN⁷

¹School of Electrical & Computer Engineering, Purdue University, West Lafayette, Indiana 47907, United States

²Purdue Quantum Science and Engineering Institute, Purdue University, West Lafayette, Indiana 47907, United States

³FMN Laboratory, Bauman Moscow State Technical University, Moscow 105005, Russia

⁴Dukhov Automatics Research Institute (VNIIA), Moscow 127055, Russia

⁵Institute for Theoretical and Applied Electromagnetics RAS, Moscow 125412, Russia

⁶Centre for Nano Optics, University of Southern Denmark, Campusvej 55, DK-5230 Odense M, Denmark

⁷Johns Hopkins University, Baltimore, Maryland 21218, USA

*Corresponding author: shalaev@purdue.edu

Published 7 May 2020

This document provides supplementary information to “Ultrafast quantum photonics enabled by coupling plasmonic nanocavities to strongly radiative antennas,” <https://doi.org/10.1364/OPTICA.382841>. The structural details of nanocube photomodification are provided. The radiative rate of a plasmonic mode is derived as a function of its volume and the plasma frequency. The effective antenna and cavity volumes of the hybridized mode are expressed as a function of antenna and cavity mode volumes. Finally, we outline the details of the numerical simulations.

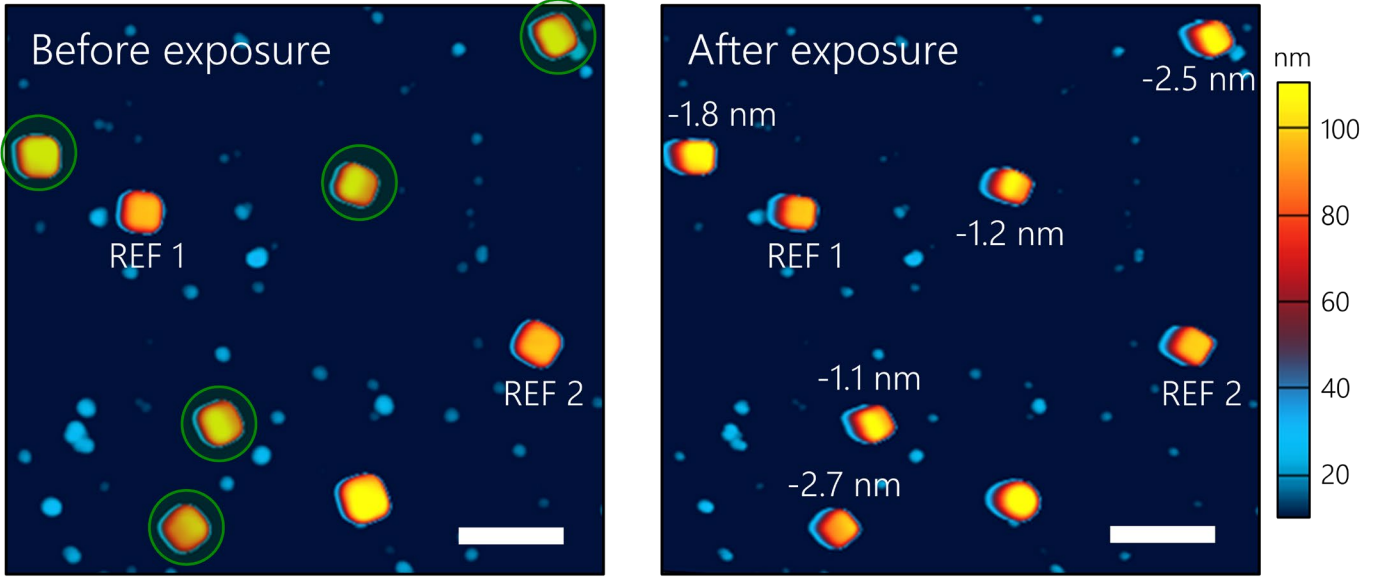
Structural characterization of photomodification. While the photomodification of nanoantennas has been reported previously, we aim here at quantitatively determining the geometric modification of the nanoantennas in our experimental conditions. A reference experiment was conducted with the idea to determine nanocube height before and after laser treatment. We took a piece of silicon substrate covered epitaxially with silver similar to the one described in the main text. A droplet of water solution with nanodiamonds was deposited on the silver piece resulting in a coverage with a density of 60 ± 8 particles per μm^2 . Subsequently, a droplet of an ethanol solution containing nanocubes was casted on the substrate, resulting a nanocube coverage of approximately 1 per μm^2 (see **Supplementary Figure 1**).

The randomly assembled nanopatch antennas were first scanned with an atomic force microscope (AFM). The profiles of the nanocubes were recorded and they were divided into two categories. The nanocubes with no appreciable tilt were labeled as reference particles (REF 1 and REF 2) and were not going to be

exposed to the intense laser light. The nanocubes exhibiting a tilt were subject to a photomodification procedure consisting in an irradiation with 1 mW laser power for 1 minute per nanocube. The laser power was measured before the beam entered the objective. This irradiation power corresponds to an optical intensity on the order of 10^4 W/cm². After the photomodification, the same area of the sample was rescanned by the AFM and the nanocube height was recorded for every particle. The systematic change in height of reference particles (+ 1.4 nm for REF 1 and +1.5 nm for REF 2) can be attributed to a difference in tip-sample force interactions in two measurements. [S1]. We corrected the height change recorded on the exposed nanocubes with this offset. With this correction, in all the cases, we recorded a negative change in nanocube height after laser irradiation, ranging from -1.1 nm to -2.7 nm, averaging at -1.9 nm. This change in height corresponds to approximately 1.5° change in the tilt angle for the nanocube. One cube in the bottom half of the image shows a notable shape change symptomatic of its displacement during the scan. This displacement occurs when

certain cubes are weakly attached to the sample surface. Therefore, we disregarded this cube in our study.

Now we recall that by definition, $V_{\text{eff}} = \left| \int \mathbf{E}(\mathbf{r}) d^3\mathbf{r} \right|^2 / \int |\mathbf{E}(\mathbf{r})|^2 d^3\mathbf{r}$. Combining the above equations, we express the radiative emission



Supplementary Figure 1. AFM images of nano-patch antennas before (left panel) and after (right panel) exposure with 1 mW incident laser power. Nanodiamonds appear as 20 nm high particles of cyan color. Green circles show on the left panel the antennas subjected to laser treatment, while the unmodified antennas are labeled as REF 1 and REF 2. The numbers next to the modified antennas represent the measured changes in nanocube heights. The scale bar in both images represents 500 nm.

Radiative rate of a plasmonic mode. Let us consider a subwavelength plasmonic mode with effective volume V_{eff} radiating its energy into the far-field. Its radiative rate can be expressed as $\gamma_{\text{rad}} = P_{\text{rad}}/U$, where P_{rad} is the instantaneous radiative power at a given moment and U is the energy stored in the mode at that same moment. Let us now express both these quantities in terms of the material properties of the plasmonic material giving rise to the mode. Let us assume that the material possesses an electronic density n and an effective electronic mass m_{eff} associated with a plasma frequency $\omega_p = (nq^2/\epsilon_0 m_{\text{eff}})^{1/2}$. Let us note as \mathbf{p} the dipolar moment that the mode possesses. Then, the instantaneous radiative power can be expressed [S2] as:

$$P_{\text{rad}} = \frac{|\mathbf{p}|^2 \omega^4}{12\pi\epsilon_0 c^3} \quad (1)$$

The dipole moment \mathbf{p} is the sum of the dipole moments of all individual oscillating electrons:

$$\mathbf{p} = \int n \frac{q^2 \mathbf{E}(\mathbf{r})}{m\omega^2} d^3\mathbf{r} \quad (2)$$

where $\mathbf{E}(\mathbf{r})$ is the amplitude of the electric field at the point \mathbf{r} and the integration is carried over the infinite three-dimensional space. Meanwhile, the energy stored in the mode is distributed between the kinetic energy of the electrons and that of the oscillating electric field, neglecting a small part stored in the magnetic energy. At the moment when the electric field is zero, we can compute the total mode energy as the sum of the electron's kinetic energies:

$$U = \int n \frac{q^2 |\mathbf{E}(\mathbf{r})|^2}{2m\omega^2} d^3\mathbf{r} \quad (3)$$

rate as $\gamma_{\text{rad}} = \frac{\omega_p^2 V_{\text{eff}}}{\omega V_0}$, where $V_0 = 3\lambda^3/4\pi^2$.

Effective cavity and antenna volumes. We justify the expressions $V_c = 2V_1$ and $V_A = (\sqrt{V_1} + \sqrt{V_2})^2/2$ used in the main text to represent the effective antenna and cavity volumes of the coupled mode a_+ . If the total energy in the coupled mode a_+ is U then the energy in the smaller mode a_1 is $U_1 = U/2$. Then, to express the Purcell factor, we can write

$$F_+ = \frac{3}{4\pi^2} \left(\frac{\lambda}{n} \right)^3 \frac{Q_+}{V_c} \quad (4)$$

where $V_c = 2V_1$ is the **effective cavity volume**, i.e. the volume defining the field concentration in the smaller mode where the QE is placed. Next, we want to find the expression for the effective dipole moment. We notice the relation between the dipole moments of the modes and the energies contained in those modes

$$p_{1,2} = \frac{\omega_p}{\omega} \sqrt{2A\epsilon_0 U_{1,2} V_{1,2}} \quad (5)$$

where A is of the order of unity, depending on geometry. For example, for spherical nanoparticles $A=3$, while for a gap mode (essentially a plane parallel capacitor), $A=1$. Therefore, the square of the total dipole moment of the coupled mode is

$$p_+^2 = |\mathbf{p}_1 + \mathbf{p}_2|^2 = 2 \frac{\omega_p^2}{\omega^2} A\epsilon_0 U V_A \quad (6)$$

where the **effective antenna volume** is

$$V_A = \frac{1}{2} |\hat{p}_1 V_1^{1/2} + \hat{p}_2 V_2^{1/2}|^2 \quad (7)$$

For the nanopatch fundamental modes, the dipole moments are aligned and therefore, we can simply write $V_A = \frac{1}{2} (\sqrt{V_1} + \sqrt{V_2})^2$.

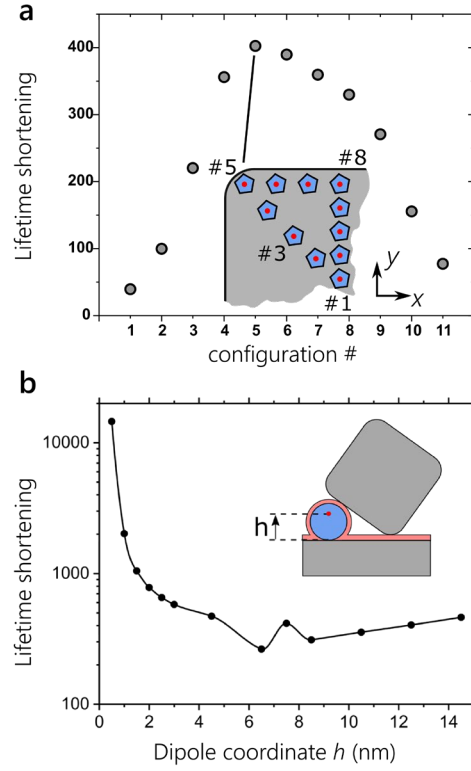
Thus, the coupled mode a_+ has a small effective volume as a cavity, yet a large effective volume as an antenna.

Mode volumes in the assembled NPA. We approximate the mode volumes in the experimentally investigated NPA as the volumes of the resonators themselves corrected by the depth of the skin layer in silver. In reference [S3], the skin depth for silver is calculated to be 25 nm. Taking into account that the losses in our crystalline silver are over 2 times lower than in [S3] (as reported in references [S4] and [S5]), we estimate the skin depth in our silver to be about $\delta_s \approx 10$ nm.

In the estimate of the unmodified cavity volume, we assume that the cavity mode occupies the entire gap space under the tilted cube. In the estimate corresponding to $\theta = 0^\circ$, we assume that the cavity mode is localized to the nanodiamond. The measured cube length being $L = 104$ nm and the diamond diameter being $d_{ND} \approx 17$ nm, we find $v_1(12^\circ) \approx (L^2 \delta_s + L^2 \delta_s \cos \theta + 0.5L^3 \cos \theta \sin \theta) / V_0 \approx 1.4 \cdot 10^{-2}$ for $\theta = 12^\circ$ and $v_1(0^\circ) \approx \frac{4}{3V_0} \pi \left(\frac{d_{ND}}{2} + \delta_s \right)^3 \approx 10^{-3}$ for $\theta = 0^\circ$. The antenna mode on the other hand has a volume of $v_2 \approx (L^3 - (L - 2\delta_s)^3) / V_0 \approx 0.02$.

Effect of dipole position inside the NPA. We simulated the total decay rate enhancement of a nanodiamond-based NV center in an NPA depending on the ND location under the nanocube (see Supplementary Figure 2(a)). Out of the 11 simulated configurations, the largest enhancement of over 400 times was exhibited by the configuration #5, in which the nanodiamond was positioned under a corner of the nanocube. In this simulation, we assumed a vertical optical dipole emitting at a wavelength of 650 nm and oriented along the z axis, located in the center of a spherical nanodiamond with diameter 15 nm. The nanocube tilt was adjusted accordingly for each of the 11 nanodiamond positions. The enhancement was calculated with respect to a reference configuration with the same nanodiamond positioned on a glass substrate with index $n_{\text{glass}} = 1.515$.

Additionally, we have simulated the decay rate enhancement as a function of the vertical position of the dipole inside the diamond (see Supplementary Figure 2(b)). This position can play an important role in both the observed total decay rate and far-field collected photon intensity. Expectedly, as the dipole approaches the silver surface, the decay rate diverges due to efficient quenching, i.e. nonradiative energy dissipation in the metal.

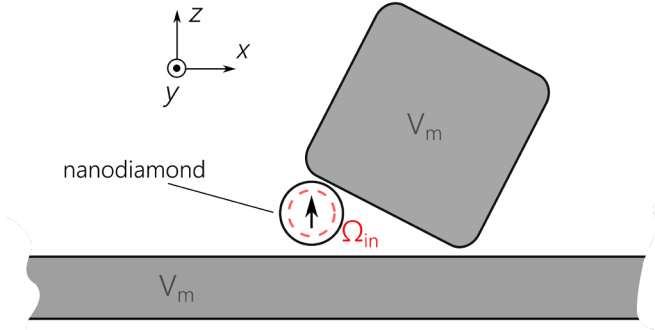


Supplementary Figure 2. (a) Dependence of the NV decay rate enhancement on the in-plane position of the ND within the NPA. The enhancement is calculated relative to an NV in a nanodiamond on glass substrate with index $n_{\text{glass}} = 1.515$. (b) Dependence of the NV decay rate enhancement on the position of the NV within the nanodiamond along the z axis for the NPA configuration #5 from (a).

Details of numerical simulations. The numerical electromagnetic calculations were performed using finite-element time-domain method with a commercial solver COMSOL 5.3, Wave Optics Module. The simulation domain was a box with $2 \mu\text{m}$ base width and $3 \mu\text{m}$ height surrounded by a 400 nm thick perfectly matching layer. The optical emitter was modeled as an AC current density inside a 200 pm diameter sphere enclosed by a 15 nm diameter diamond shell with $n_{\text{diam}} = 2.42$. The emitter dipole was oriented out of-plane (along the z axis) and its wavelength was varied between 500 and 900 nm. The nanodiamond particle with the embedded dipole was sitting on a 100 nm thick epitaxial Ag layer and conformally covered with a 5 nm thick alumina layer ($n_{\text{Al}_2\text{O}_3} = 1.68$). A silver nanocube with a 100 nm edge length was placed on top of the nanodiamond. The nanocube corners had an 11 nm radius of curvature and the nanocube was further conformally covered in a 3 nm thick PVP layer with the index $n_{\text{PVP}} = 1.4$. The bottom facet of the nanocube was tangent to the nanodiamond particle and the edge of the bottom facet furthest from the nanodiamond was resting on the alumina spacer. The dipole emitter was introduced as a volume current density coherently oscillating inside a 100-pm-radius sphere. The total decay rate is calculated as the surface integral of total power flow \mathbf{P} through the 300-pm-radius spherical surface Ω_{in} , surrounding the emitting dipole and situated entirely within the nanodiamond volume (see Supplementary Figure 3): $\gamma_{\text{tot}} = \int_{\Omega_{\text{in}}} \mathbf{P} \cdot d\mathbf{S}$.

The loss rate is calculated as the total work performed by the electric field on the free charges of the nanocube and a portion of the

metallic substrate within 750 nm from the emitter, occupying the volume $V_m : \gamma_{\text{loss}} = \int_{V_m} \mathbf{j} \cdot \mathbf{E} dV$.

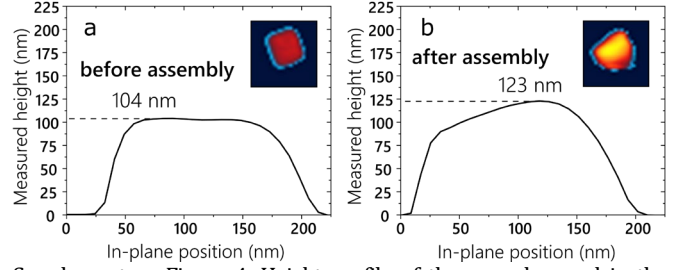


Supplementary Figure 3. Schematic illustration of integration volume and surface used for simulating the total decay rates and optical loss rates of quantum dipoles coupled to NPAs.

Experimental setup. The deterministic assembly of the NPA was performed using an atomic force microscope (Cypher S, Oxford Instruments). Optical characterization experiments were performed on a home-built scanning confocal microscope with a 50 μm pinhole based on a commercial inverted microscope body (Nikon Ti-U). Objective scanning was performed by a P-561 piezo stage driven by an E-712 controller (Physik Instrumente) equipped with a scriptable, interactive workstation built in LabVIEW on Physik Instrumente's open-source libraries for positioning and native photonic scan/alignment functionalities. The optical pumping in the continuous wave (CW) experiments was by a 200 mW continuous wave 532 nm laser (Shanghai Laser Century). The diameter of the beam incident on the objective was 12 mm, while that of the objective back aperture was 3 mm. Accounting for the objective NA of 0.9, its aberrations and the $M^2 = 1.2$ of the pump laser, we estimate that the pump spot size on the sample was around 1 μm . The CW measured autocorrelation was fitted by a standard two-exponential model $g^{(2)}(\tau) = 1 - A \exp(-|\tau|/\tau_A) + B \exp(-|\tau|/\tau_B)$. Pulsed fluorescence lifetime measurements were performed using a 508 nm picosecond laser with a nominal 20 MHz repetition rate (BDL SMNi, Becker&Hickl). Time-correlated histograms were acquired with an SPC-150 time-correlated photon counting system (acquisition card with a 4 ps internal jitter) based on a start-stop method. The excitation beam was reflected off a 550 nm long-pass dichroic mirror (DMLP550L, Thorlabs), and a 550 nm long-pass filter (FEL0550, Thorlabs) was used to filter out the remaining pump power. After passing through the pinhole, two avalanche detectors with a 30 ps time resolution and 35% quantum efficiency at 650 nm (PDM, Micro-Photon Devices) were used for single-photon detection during time-correlated measurements. An avalanche detector with 69% quantum efficiency at 650 nm (SPCM-AQRH, Excelitas) was used for scanning and saturation measurements. The saturation curves reflecting the dependence of fluorescence intensity I on pump power P have been fitted with the formula $I = I_{\text{sat}} P / (P + P_{\text{sat}})$. The instrument response function (IRF) of our time-resolved setup was measured using the attenuated reflection of the pulsed ps laser.

Nanocube tilt measurements. The initial inclination angle and the diamond size were obtained from the AFM data acquired at the assembly stage (see Supplementary Figure 3 below). Knowing the initial cube height ($h_{\text{NC}} = 104 \pm 1$ nm) and the height change during

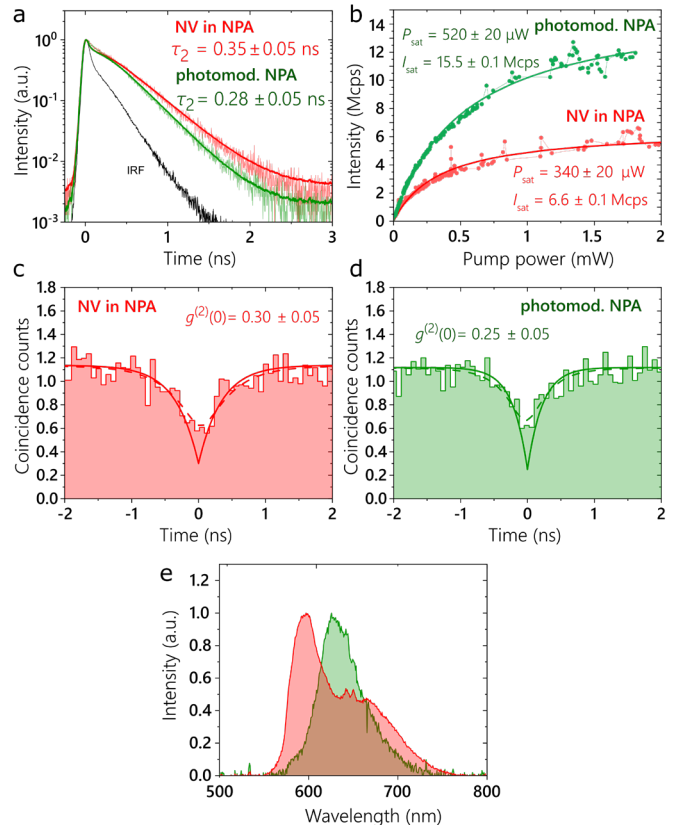
the assembly of the inclination angle was found to be. Note that the angle obtained from directly fitting the measured profile of the cube's upper surface would be different. We rely on the change in cube's height as this is the only parameter that can be reliably extracted from the AFM measurements.



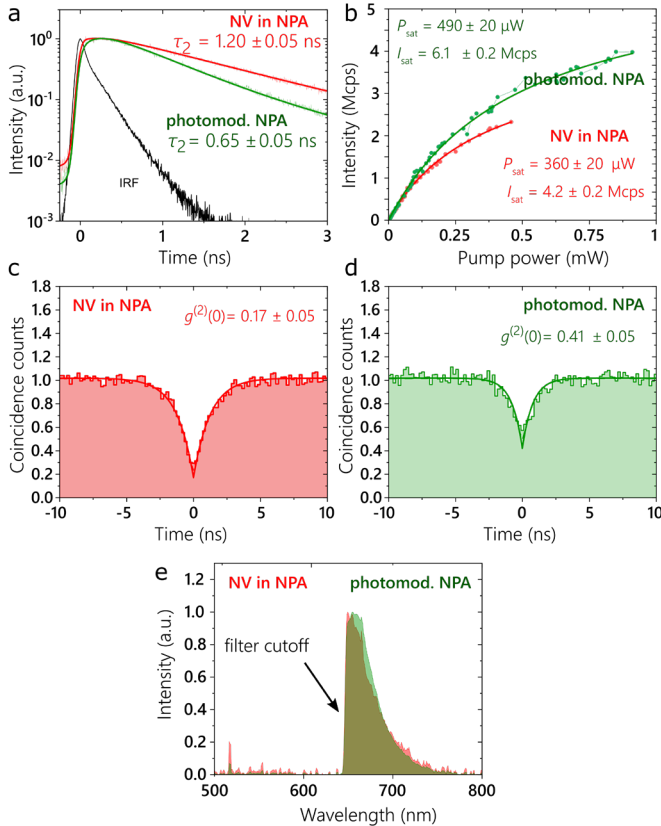
Supplementary Figure 4. Height profile of the nanocube used in the deterministic NPA assembly (a). Height profile of the assembled NPA with a nanodiamond underneath the cube (b). The tilt of the upper cube's surface is around 12° based on the change of cube's height. Insets show the two-dimensional nanocube height profiles.

Our reference photomodification experiments show that the cube height change is about 2 nm on average as a result of laser treatment. Using this value we roughly estimate that the modified cube's tilt angle should be between 9 and 11 degrees.

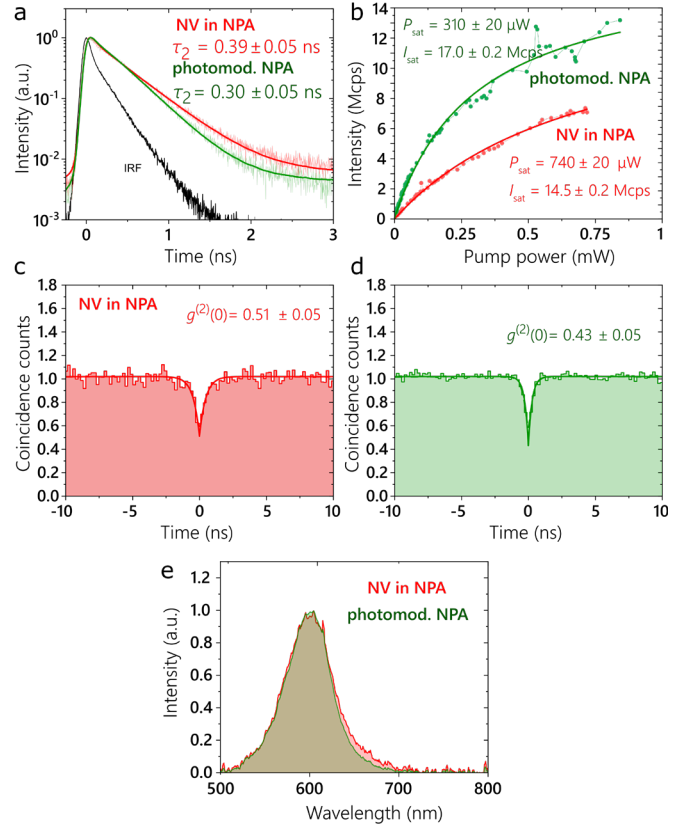
Data from additional photomodified NPAs. In Supplementary Figures 3, 4 and 5, we plot the characterization details of additional (randomly assembled) NPAs that were successfully photomodified to produce enhanced performance. This data was obtained prior to performing the deterministic photomodification experiment. We observe a shortening of fluorescence lifetime and an increase in brightness. In agreement with the NPA geometry change, Supplementary Figure 3(e) shows that the emission spectrum is significantly red-shifted after photomodification.



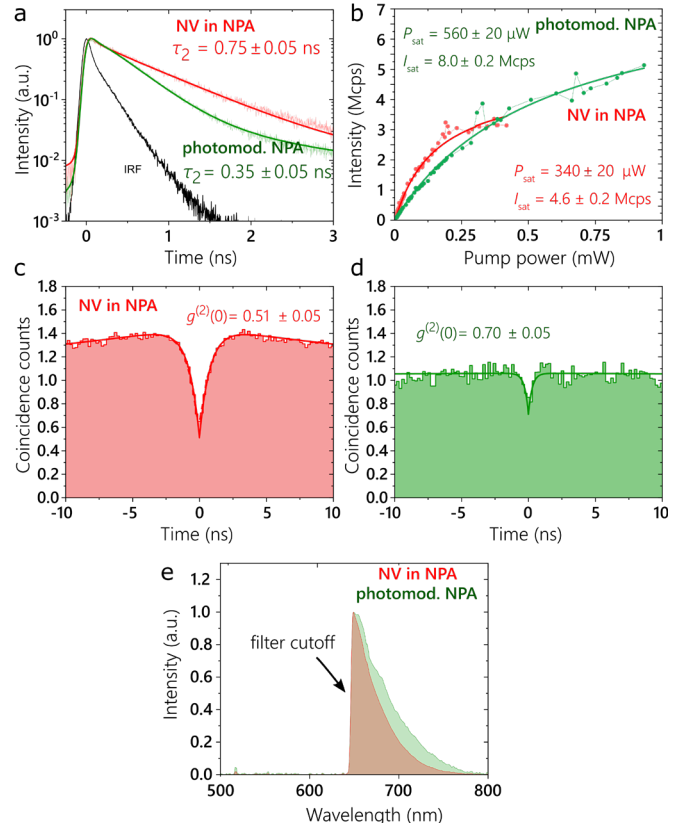
Supplementary Figure 5. Photomodification procedure demonstrated on a randomly assembled NPA. (a) Fluorescence lifetime measurements with the instrument response function (IRF) shown as a black line. (b) Fluorescence saturation measurements (c-d) photon autocorrelation measurements with a detector-limited resolution of 260 ps. The experimental data is shown as a bar plot, while the convoluted fit is shown as a dashed line. (e) fluorescence spectra.



Supplementary Figure 6. Photomodification procedure demonstrated on a randomly assembled NPA 2. (a) Fluorescence lifetime measurements with the instrument response function (IRF) shown as a black line. (b) Fluorescence saturation measurements (c-d) photon autocorrelation measurements with a bin-limited resolution of 190 ps. The experimental data is shown as a bar plot, while the convoluted fit is shown as a dashed line. (e) fluorescence spectra.



Supplementary Figure 7. Photomodification procedure demonstrated on a randomly assembled NPA 3. (a) Fluorescence lifetime measurements with the instrument response function (IRF) shown as a black line. (b) Fluorescence saturation measurements (c-d) photon autocorrelation measurements with a bin-limited resolution of 190 ps. (e) fluorescence spectra.



Supplementary Figure 8. Photomodification procedure demonstrated on a randomly assembled NPA 3. (a) Fluorescence lifetime

measurements with the instrument response function (IRF) shown as a black line. (b) Fluorescence saturation measurements (c-d) photon autocorrelation measurements with a bin-limited resolution of 190 ps. (e) fluorescence spectra.

References

- S1. J. Legleiter, "The effect of drive frequency and set point amplitude on tapping forces in atomic force microscopy: simulation and experiment," *Nanotechnology* **20**, 245703 (2009).
- S2. L. Novotny and B. Hecht, "Principles of Nano-Optics by Lukas Novotny," Cambridge University Press (2012).
- S3. H. U. Yang, J. D'Archangel, M. L. Sundheimer, E. Tucker, G. D. Boreman, and M. B. Raschke, "Optical dielectric function of silver," *Phys. Rev. B* **91**, 235137 (2015).
- S4. S. I. Bogdanov, M. Y. Shalaginov, A. S. Lagutchev, C.-C. Chiang, D. Shah, A. S. Baburin, I. A. Ryzhikov, I. A. Rodionov, A. V. Kildishev, A. Boltasseva, and V. M. Shalaev, "Ultrabright Room-Temperature Sub-Nanosecond Emission from Single Nitrogen-Vacancy Centers Coupled to Nanopatch Antennas," *Nano Letters* **18**, 4837–4844 (2018).
- S5. I. A. Rodionov, A. S. Baburin, A. R. Gabidullin, S. S. Maklakov, S. Peters, I. A. Ryzhikov, and A. V. Andriyash, "Quantum Engineering of Atomically Smooth Single-Crystalline Silver Films," *Sci Rep* **9**, 12232 (2019).